31. G. M. Culver, J. H. Cate, G. Zh. Yusupova, M. M. Yusupov, H. F. Noller, *Science* **285**, 2133 (1999).
32. R. A. Garrett and C. Rodriguez-Fonseca, in *Ribosomal RNA: Structure, Evolution, Processing and Function in Protein Biosynthesis*, R. A. Zimmerman and A. E. Dahlberg, Eds. (CRC Press, Boca Raton, FL, 1996), pp. 327–355.
33. A. A. Szewczak and P. B. Moore, *J. Mol. Biol.* **247**, 81 (1995).
34. C. C. Correll *et al.*, *Proc. Natl. Acad. Sci. U.S.A.* **95**, 13436 (1998).
35. I. G. Wool, A. Gluck, Y. Endo, *Trends Biochem. Sci.* **17**, 266 (1992).
36. D. Moazed, J. M. Roberston, H. F. Noller, *Nature* **334**, 362 (1988).
37. C. C. Correll, B. Freeborn, P. B. Moore, T. A. Steitz, *Cell* **91**, 705 (1997).
38. S. Gerbi, in *Ribosomal RNA: Structure, Evolution, Processing and Function in Protein Biosynthesis*, R. A. Zimmermann and A. E. Dahlberg, Eds. (CRC Press, Boca Raton, FL, 1996), pp. 71–88.
39. P. Dube *et al.*, *Structure* **6**, 389 (1998).
40. V. C. Ware *et al.*, *Nucleic Acids Res.* **22**, 7795 (1983).
41. P. B. Moore, *Annu. Rev. Biochem.* **68**, 287 (1999)
42. E. Westhof and V. Fritsch, *Structure* **8**, R55 (2000).
43. A. Nakagawa *et al.*, *EMBO J.* **18**, 1459 (1999).
44. M. Wahl, R. Huber, M. C. Wahl, *EMBO J.* **19**, 807 (2000).
45. R. Beckmann *et al.*, *Science* **278**, 2123 (1997).
46. M. G. Rossmann and J. E. Johnson, *Annu. Rev. Biochem.* **58**, 533 (1989); A. Liljas, *Int. Rev. Cytol.* **124**, 103 (1991).
47. K. Lugor *et al.*, *Nature* **389**, 251 (1997).
48. H. S. Chittum and W. S. Champney, *J. Bacteriol.* **176**, 6192 (1994).
49. B. Lee and F. M. Richards, *J. Mol. Biol.* **55**, 379 (1971).
50. R. K. Agrawal *et al.*, *J. Biol. Chem.* **274**, 8723 (1999).
51. E. V. Puglisi, R. Green, H. F. Noller, J. D. Puglisi, *Nature Struct. Biol.* **4**, 775 (1997).
52. M. A. Rould, J. J. Perona, D. Söll, T. A. Steitz, *Science* **246**, 1135 (1989).
53. A. Shevack, H. S. Gewitz, B. Hennemann, A. Yonath, H. G. Wittmann, *FEBS Lett.* **184**, 68 (1985).
54. K. vanBohlen *et al.*, *J. Mol. Biol.* **222**, 11 (1991).
55. Z. Otwinowski, in *Data Collection and Processing*, L. Sawyer, N. Isaacs, D. Bailey, Eds. (SERC Daresbury Laboratory, Warrington, UK, 1993), pp. 52–62.
56. E. de La Fortelle and G. Bricogne, *Methods Enzymol.* **276**, 472 (1997).
57. T. A. Jones, S. Cowan, J.-Y. Zou, M. Kjeldgaard, *Acta Crystallogr.* **A46**, 110 (1991).
58. B. L. Golden, V. Ramakrishnan, S. W. White, *EMBO J.* **12**, 4901 (1993).
59. M. A. Markus, A. P. Hinch, S. Huang, D. E. Draper, D. E. Torchia, *Nature Struct. Biol.* **4**, 70 (1997).
60. M. Leijonmarck, S. Eriksson, A. Liljas, *Nature* **286**, 824 (1980).
61. C. Davies, S. W. White, V. Ramakrishnan, *Structure* **4**, 55 (1996).
62. J. Unge *et al.*, *Structure* **6**, 1577 (1998).
63. K. S. Wilson, K. Appelt, J. Badger, I. Tanaka, S. W. White, *Proc. Natl. Acad. Sci. U.S.A.* **83**, 7251 (1986).
64. P. Nissen, J. Hansen, N. Ban, P. B. Moore, T. A. Steitz, *Science* **289**, 920 (2000).
65. R. R. Gutell *et al.*, in preparation. (Data can be found at www.rna.icmb.utexas.edu.)
66. M. Symanski, T. Specht, M. C. Barciszewska, J. Barciszewski, V. A. Erdmann, *Nucleic Acids Res.* **26**, 156 (1998).
67. M. Carson, *Methods Enzymol.* **277**, 493 (1997).

68. We thank B. Freeborn for her skilled technical assistance in preparing 50*S* ribosomal subunit material and crystals. We are indebted to D. Klein, M. Lu, S. Antoć, and M. Schmeing for their help with the fitting of protein sequences into electron density. We thank M. Kjeldgaard for providing us with a prerelease version of O adapted for RNA model building, J. Cate for contributing the iridium hexamine, R. Gutell and J. Cannone for preparing the secondary structure diagram for 23*S* rRNA, M. Wahl for sending us coordinates for L4 before their release, J. Williamson for sending us coordinates of the L30e-RNA complex before their release, R. Sweet, L. Berman, and M. Capel for their assistance with data collection at the National Synchrotron Light Source, and A. Joachimiak and the staff of 19ID at the Advanced Photon Source. Supported by grants from NIH to T.A.S. (GM22778) and P.B.M. (GM54216) and by a grant from the Agouron Institute to T.A.S. and P.B.M. N.B. is supported by a Burroughs Welcome Fund Career Award. Complete coordinates for 23*S* and 5*S* rRNAs and α carbon coordinates for the 27 proteins discussed have been deposited in the Protein Data Bank. The accession number is 1FFK for the amplitudes, experimental phases, and coordinates.

29 June 2000; accepted 24 July 2000

The Structural Basis of Ribosome Activity in Peptide Bond Synthesis

Poul Nissen,[1]* Jeffrey Hansen,[1]* Nenad Ban,[1]* Peter B. Moore,[1,2] Thomas A. Steitz[1,2,3]

Using the atomic structures of the large ribosomal subunit from *Haloarcula marismortui* and its complexes with two substrate analogs, we establish that the ribosome is a ribozyme and address the catalytic properties of its all-RNA active site. Both substrate analogs are contacted exclusively by conserved ribosomal RNA (rRNA) residues from domain V of 23*S* rRNA; there are no protein side-chain atoms closer than about 18 angstroms to the peptide bond being synthesized. The mechanism of peptide bond synthesis appears to resemble the reverse of the acylation step in serine proteases, with the base of A2486 (A2451 in *Escherichia coli*) playing the same general base role as histidine-57 in chymotrypsin. The unusual pK_a (where K_a is the acid dissociation constant) required for A2486 to perform this function may derive in part from its hydrogen bonding to G2482 (G2447 in *E. coli*), which also interacts with a buried phosphate that could stabilize unusual tautomers of these two bases. The polypeptide exit tunnel is largely formed by RNA but has significant contributions from proteins L4, L22, and L39e, and its exit is encircled by proteins L19, L22, L23, L24, L29, and L31e.

It has been known for 35 years that the peptidyl transferase activity responsible for the peptide bond formation that occurs during messenger RNA (mRNA)–directed protein synthesis is intrinsic to the large ribosomal subunit (*1–4*), and it has been understood for even longer that the ribosome contains proteins as well as RNA. In bacteria, for example, the large ribosomal subunit contains ~35 different proteins and two RNAs (*5, 6*). These findings pose three related questions: (i) which of the macromolecular components of the large ribosomal subunit contribute to its peptidyl transferase site, (ii) where is that site located, and (iii) how does it work?

By 1980, the list of components that might be part of the ribosome's peptidyl transferase center had been reduced to about a half dozen proteins and 23*S* rRNA [for reviews, see (*7, 8*)]. Following the discovery of catalytic RNAs (*9, 10*), the hypothesis that 23*S* rRNA might be its sole constituent, which had been proposed years earlier (*11*), began to gain favor. In 1984, Noller and colleagues published affinity-labeling results that showed that U2619 and U2620 (U2584 and U2585, respectively, in *E. coli*; hereafter, bases in parenthesis indicate the corresponding position in *E. coli* rRNA) are adjacent to the CCA-end of P site–bound transfer RNA (tRNA) (*12, 13*). These nucleotides are part of a highly conserved internal loop in the center of domain V of 23*S* rRNA. The hypothesis that this loop is intimately involved in the peptidyl transferase activity was supported by the observation that mutations in that loop render cells resistant to many inhibitors of peptidyl transferase, and evidence implicating it in this activity has continued to mount (*14, 15*).

Definitive proof that the central loop in domain V is the sole component of the ribosome involved in the peptidyl tranferase activity has remained elusive, however. In the 1990s, Noller and colleagues prepared particles that retain peptidyl transferase activity by increasingly vigorous deproteinizations of large ribosomal subunits, but active particles that were completely protein-free could not be produced (*16, 17*). Nevertheless, combined with earlier reconstitution results (*18*), this work reduced the number of proteins that might be involved to just two: L2 and L3 (*19*). More recently, Watanabe and co-workers reported success in eliciting peptidyl transferase activity from in vitro–synthesized, protein-free 23*S* rRNA (*20, 21*), but their observations have not withstood further scrutiny (*22*). Thus, the question still re-

[1]Department of Molecular Biophysics and Biochemistry and [2]Department of Chemistry, Yale University, and [3]Howard Hughes Medical Institute, New Haven, CT 06520–8114, USA.

*These authors contributed equally to this work.

mains: is the ribosome a ribozyme or is it not?

Over the years, the location of the peptidyl transferase site in the ribosome has been approached almost exclusively by electron microscopy. In the mid-1980s, evidence began to accumulate that there is a tunnel running through the large ribosomal subunit from the middle of its subunit interface side to its back (*23, 24*), and there was, and still is, strong reason to believe that polypeptides pass through it as they are synthesized (*25–27*). More recent cryo-electron microscopic investigations (*28–31*) have confirmed the existence of the tunnel and have demonstrated that the CCA ends of ribosome-bound tRNAs bound to the A (aminoacyl)- and P (peptidyl)-sites are found in the subunit interface end of the tunnel. Consequently, the peptidyl transferase site must be located at that same position, which is at the bottom of a deep cleft in the center of the subunit interface surface of the large subunit, immediately below its central protuberance.

The substrates of the reaction catalyzed by the large subunit are an aminoacyl-tRNA (aa-tRNA) and a peptidyl-tRNA. The former binds in the ribosome's A-site and the latter in its P-site. The α-amino group of the aa-tRNA attacks the carbon of the carbonyl acylating the 3′ hydroxyl group of the peptidyl-tRNA, and a tetrahedral intermediate is formed at the carbonyl carbon (Fig. 1). The tetrahedral intermediate resolves to yield a peptide extended by one amino acid esterified to the A site–bound tRNA and a deacylated tRNA in the P-site.

This reaction scheme is supported by the observations of Yarus and colleagues (*32*) who synthesized an analog of the tetrahedral intermediate by joining an oligonucleotide having the sequence CCdA to puromycin via a phosphoramide group (Fig. 1). The sequence CCA, which is the 3′-terminal sequence of all tRNAs, binds to the large subunit by itself, consistent with the biochemical data showing that the interactions between tRNAs and the large subunit largely depend on their CCA sequences (*33, 34*). Puromycin is an aa-tRNA analog that interacts with the ribosomal A-site, and the phosphoramide group of the Yarus compound mimics the tetrahedral carbon intermediate. This analog, CCdA-phosphate-puromycin (CCdA-p-Puro), binds tightly to the ribosome, and inhibits its peptidyl transferase activity (*32*).

Although the structure of the large ribosomal subunit has now been determined at atomic resolution (*35*), experience with other enzymes shows that this information alone is usually insufficient for discovering catalytic mechanism. That level of understanding is achieved only when the structure of the enzyme complexed with substrates and substrate analogs has been determined.

Accordingly, we have made crystals of *Haloarcula marismortui* 50*S* ribosomal subunit complexed either with the Yarus analog, CCdA-p-Puro, or with a mini-helix analog of an aa-tRNA and have determined the structures of both complexes. The CCdA from the Yarus analog binds to the so-called P-loop (*36*), and hence is in the P-site. Only the terminal CCA of the aa-tRNA analog is visible, but because it interacts appropriately with the A-loop (*37*), it must be in the A-site. The puromycin group occupies the same location in both structures, and there are no proteins near that site. Hence, the catalytic activity of the active site must depend entirely on RNA. The N3 of A2486 (A2451) is the titratable group nearest to the peptide bond being synthesized and is likely functioning as a general base to facilitate the nucleophilic attack by the α-amino group of the A-site substrate. In order to function in this capacity, the pK_a of this base has to be roughly 5 units higher than normal. It is possible that its unusual pK_a may be produced by an interaction between A2486 (A2451) and G2482 (G2447), which in turn hydrogen bonds with the buried phosphate of A2485 (A2450). This buried phosphate can stabilize normally rare imino tautomeric forms of both bases, resulting in a "charge relay" that increases the negative charge density on the N3. When A-, P-, and E-site tRNAs are docked onto the two bound CCAs, they appear to contact proteins L10e, L5, and L44e on the central protuberance as well as 23*S* rRNA. The tunnel through which the polypeptide product passes is lined largely with RNA, but it includes a 12 Å constriction formed by portions of L4 and L22.

Structures of substrate analog complexes. In order to establish how substrates interact at the A- and P-sites of the large subunit, two substrate analogs were used. One of the analogs, which was designed to mimic the acceptor stem of an aa-tRNA and bind to the A-site, was a 12–base pair RNA hairpin with an aminoacylated, four-nucleotide extension on its 3′ end (Fig. 1). The sequence used was that of the $tRNA^{tyr}$ acceptor stem, and it is terminated with puromycin, which itself is an analog of tyrosyl-A76. The second analog used was the Yarus tetrahedral intermediate analog, CCdA-p-Puro. As in the case of the A-site substrate analog, the puromycin of the Yarus inhibitor is expected to bind at the A-site, whereas its CCdA moiety should bind at the P-site.

The positions of the Yarus inhibitor and the tRNA acceptor stem analog were determined by soaking these molecules into crystals of the *Haloarcula marismortui* 50*S* ribosomal subunit, measuring diffraction data to 3.2 Å resolution and calculating difference electron density maps (*38*). Maps of the complexes were also calculated using $2F_o$(complexed) – F_o(uncomplexed) as coefficients, to examine the shifts in the positions of ribosome residues that occur when these analogs bind (Fig. 2B and Table 1).

A model for the entire Yarus inhibitor could be fitted into the difference density (Fig. 2A), and the electron density map of the complex shows the N3 of A2486 (A2451) within hydrogen bonding distance of a nonbridging oxygen of the phosphoramide (Fig. 2B). The inhibitor's two C residues, which correspond to C74 and C75 of peptidyl-tRNA, are Watson-Crick base-paired with G2285 (G2252) and G2284 (G2251) in the P-loop, respectively (Fig. 3A). The C74-G2285 (G2252) interaction was pre-

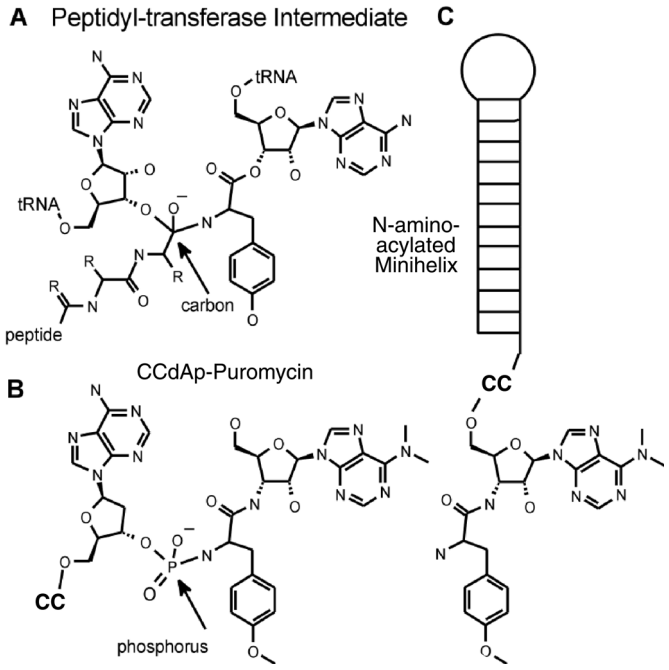

Fig. 1. Chemical structures of ribosome peptidyl transferase substrates and analogs. (**A**) The tetrahedral carbon intermediate produced during peptide bond formation; the tetrahedral carbon is indicated by an arrow. (**B**) The transition state analog formed by coupling the 3′ OH of CCdA to the amino group of the O-methyl tyrosine residue of puromycin via a phosphate group, CCdA-p-Puro (a gift from Michael Yarus) (*32*). (**C**) An *N*-amino-acylated minihelix constructed to target the A-site. The oligonucleotide sequence 5′-CCGGCGGGCUGGUUC-AAACCGGCCCGCCGGA-CC-3′ puromycin should form 13 base pairs. The construct is based on a mini-helix known to be a suitable substrate for amino-acylation by Tyr-tRNA synthetase. The 3′ OH of its terminal C is coupled to the 5′ OH of the N6-dimethyl A moiety of puromycin by a phosphodiester bond.

dicted by the results of Noller and co-workers (*39*). The dA, which corresponds to A76 of a tRNA in the P-site, is not base-paired, but rather stacks on the ribose of A2486 and hydrogen bonds to the 2′ OH of nucleotide A2485 (A2450) (Fig. 3B).

Only the CC-puromycin moiety of the mini-helix acceptor stem analog showed ordered electron density in its difference electron density map (Fig. 2C). The C75 of the acceptor stem CCA is Watson-Crick base-paired with G2588 (G2553) of the A-loop, whereas the C74 is more disordered and is not base-paired but appears to stack on a ribosome base. This interaction between C75 and G2588 is consistent with the results of Green and co-workers (*40*), who first demonstrated the functional proximity of the A-loop to the CCA end of A site–bound tRNA and who introduced the terms A-loop and P-loop. The dimethyl A of the A-site inhibitor puromycin is positioned identically to the dimethyl A of the Yarus inhibitor. Further, the dimethyl A of puromycin, which is the A76 equivalent of an A-site tRNA, interacts with the A-loop in much the same way that the A76 from the P-site CCA interacts with the P-loop (Fig. 3B). The CCAs bound in the A- and P-sites are related by a twofold axis.

The most notable of the several conformational changes in the ribosome induced by the binding of the tetrahedral intermediate analog is the ordering of base A2637 (A2602), which is disordered in the unliganded enzyme (Fig. 3B). It becomes positioned between the CCA bound at the A-site and the CCA bound at the P-site. The base of U2620 (U2585) also moves so that it can make a hydrogen bond with the 2′ hydroxyl of the ribose of A76 in the A-site, and U2619 (U2584) and G2618 (G2583) shift to allow that placement of A76. Smaller shifts are observed in the positions of A2486 (A2451), whose N3 is near to the nonbridging oxygen of the phosphate, and one of the G residues with which it interacts, G2102 (G2482).

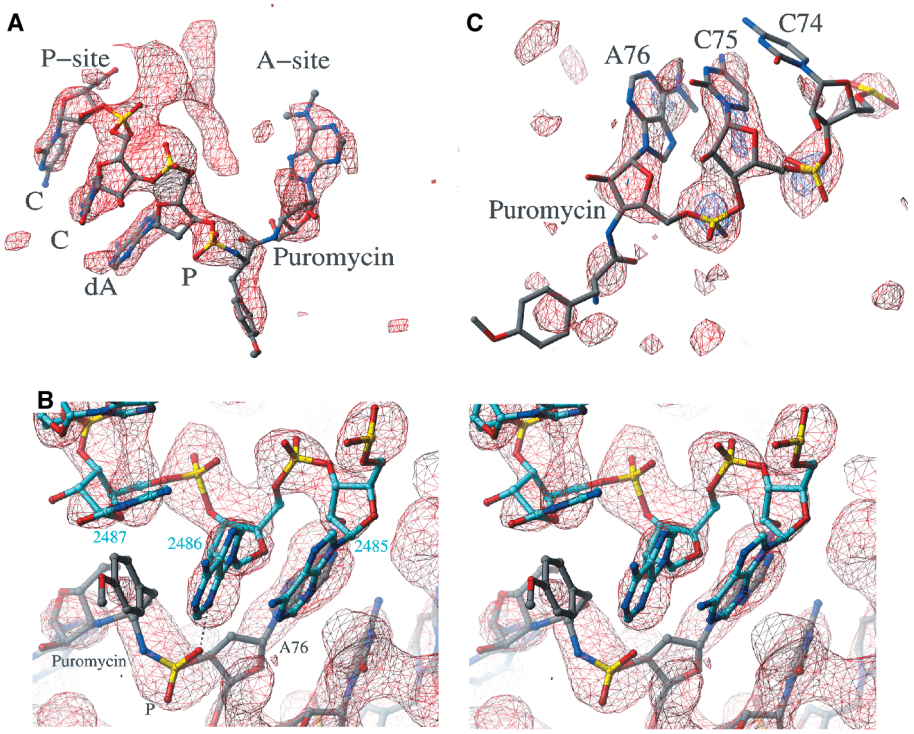

Fig. 2. Experimentally phased electron density maps of the substrate analog complexes at 3.2 Å resolution, with models superimposed (oxygen, red; phosphorus, yellow; nitrogen, blue; carbon, green for rRNA and gray for substrate). (**A**) An F_o(complex) – F_o(parent) difference electron density map with a skeletal model of CCdA-p-Puro superimposed. The CCdA corresponds to the 3′ CCA of tRNA bound to the P-site. (**B**) A stereo representation of the $2F_o$(complex) – F_o(parent) electron density map of the CCdA-p-Puro in the active site region with the structures of the ribosome and inhibitor superimposed showing the proximity of the N3 of A2486 (A2451) to the nonbridging oxygen of the inhibitor phosphoramide in this complex. (**C**) An F_o(complex) – F_o(parent) difference electron density map of the tRNA acceptor stem analog with a skeletal model of CCPuro superimposed. There is density only for the ribose and phosphate of C74 of the RNA hairpin. The CCPuro corresponds to a tyrosyl-3′ CCA of tRNA in the A-site.

Location and chemical composition of the peptidyl transferase site. The inhibitors are bound to a site made entirely of 23*S* rRNA with no proteins nearby, proving that the ribosome is a ribozyme. Both the Yarus inhibitor and the A-site analog of aa-tRNA bind to the large subunit at the bottom of a large and deep cleft at the entrance to the 100-Å-long polypeptide exit tunnel that runs through to the back of the subunit (Fig. 4). This site is surrounded by nucleotides belonging to the central loop of 23*S* rRNA domain V, the "peptidyl transferase loop." Nucleotides from the single-stranded portions of this loop make the closest approach

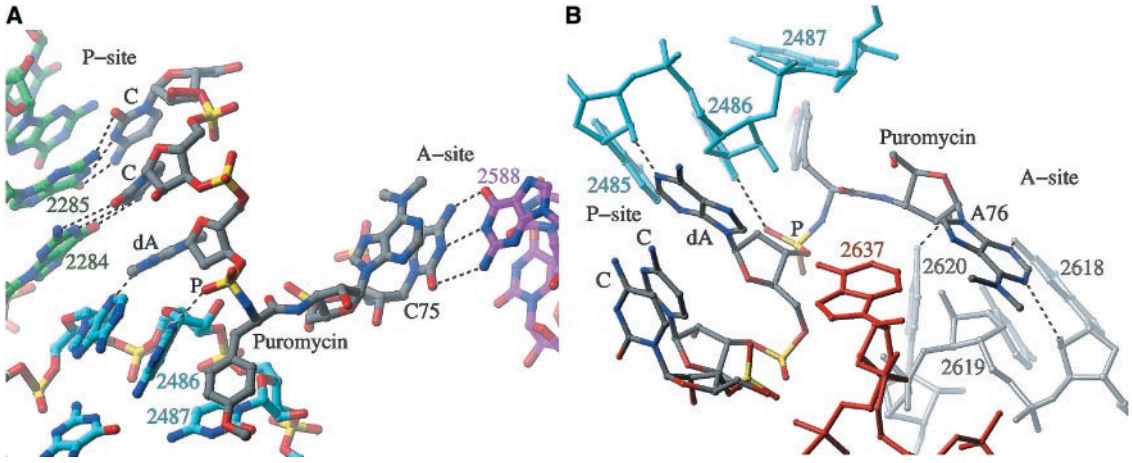

Fig. 3. A combined model of the CCA portion of the mini-helix bound to the A-site and CCdA-p-Puro bound to the A- and P-sites color coded as in Fig. 2. (**A**) The base-pairing interactions between the P-site C74 and C75 and the P-loop (green) of 23*S* rRNA on the left and the A-site C75 with the A-loop (purple) of 23*S* rRNA on the right. The catalytic A2486 (A2451) is near the phosphate oxygen (P) that is the analog of the tetrahedral intermediate oxyanion. (**B**) A view showing A2637 (A2602) (in all red) lying between the two CCA's and A2486 (blue), whose N3 approaches a nonbridging phosphate oxygen. The N1 atoms of the A76 bases from the A- and P-site tRNAs make nearly identical interactions with a ribose 2′ OH in both the A- and P-loops, respectively, and an approximate twofold axis relates these residues. The U2620 (U2585) (gray) hydrogen bonds to the 2′ hydroxyl of the A-site A76 ribose.

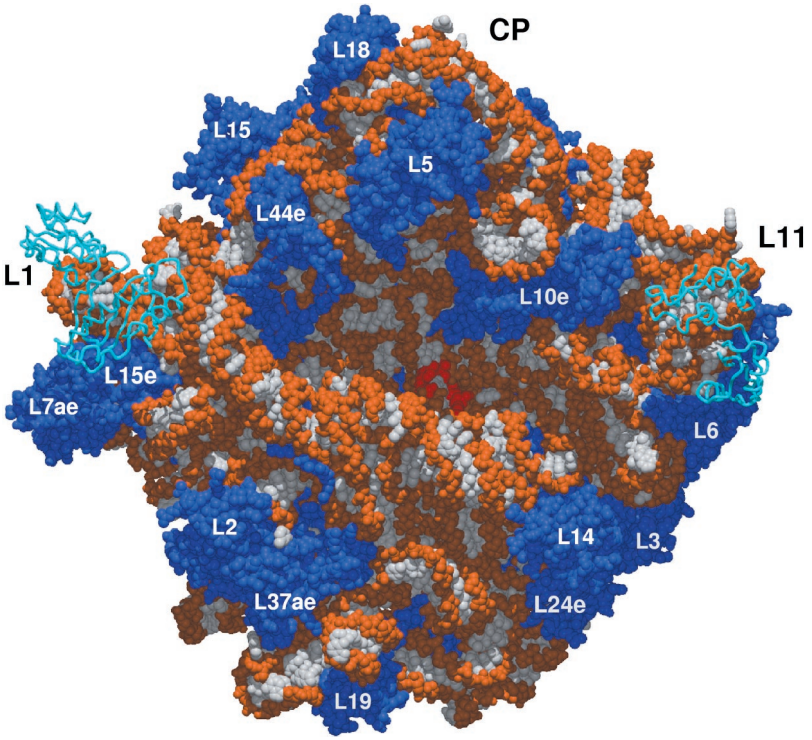

Fig. 4. A space-filling model of the 23*S* and 5*S* rRNA, the proteins, and the combined CCA models viewed down the active site cleft in a rotated "crown view." The bases are white and the sugar phosphate backbones are orange. The CCA models are red and the numbered proteins are blue. The L1 and L11 proteins positioned at lower resolution are in blue backbone. The central protuberance is labeled CP.

to the phosphate that mimics the tetrahedral carbon intermediate. In general, the helices that extend from the peptidyl transferase loop in secondary structure diagrams of 23*S* rRNA also extend away from the active site in the tertiary structure (Fig. 5). Although there are 15 proteins that interact with domain V (Fig. 6A), there are no globular proteins in the vicinity of the inhibitor. The closest polypeptides are the nonglobular extensions of several proteins (L2, L3, L4, L10e) that penetrate deeply into domain V and approach the active site (Fig. 6B). These extensions fill many of the voids between the RNA helices of domain V, neutralize phosphate backbone charge, and presumably stabilize the structure of the domain and its association with other RNA regions. However, none of their side-chain atoms is closer than about 18 Å to the phosphorus of the inhibitor's phosphate group, which marks the site where peptide bonds form. Furthermore, both substrate analogs are completely enclosed in an rRNA cavity that is so tightly packed that there is no possibility that an unidentified peptide could be lurking nearby (Fig. 7). Thus, the catalytic entity in the ribosome must be RNA.

Two of the proteins with long termini or loops penetrating the rRNA scaffold of domain V are proteins that could not previously be excluded from involvement in the peptidyl transferase reaction, L2 and L3 (*19*). Noller and

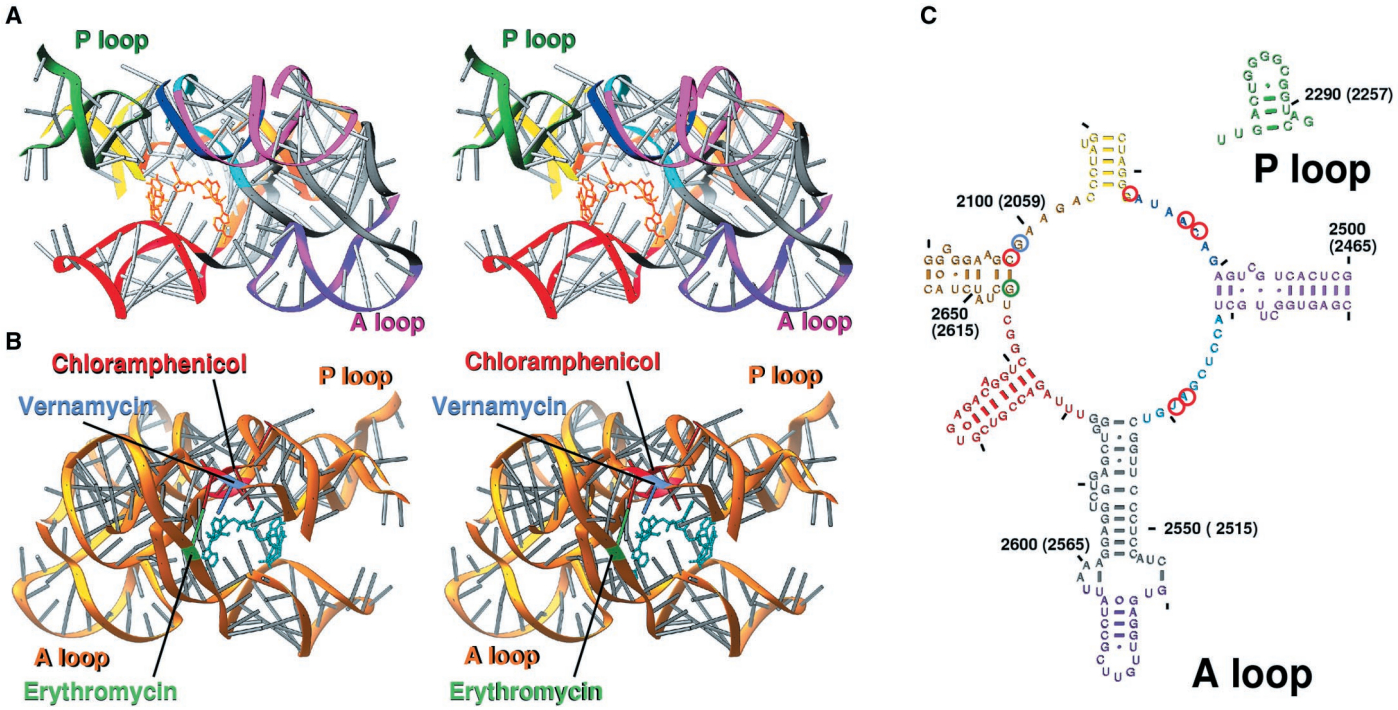

Fig. 5. Stereo drawings of the active site region of domain V and a secondary structure diagram colored to show the three-dimensional arrangement of residues comprising the A- and P-loops, the peptidyl transferase loop, and some antibody resistance mutations. The rRNA backbone is represented as ribbon and the bases as sticks. (**A**) The active site regions viewed in stereo down the active site cleft, as in Fig. 4, with the Yarus analog in yellow. The RNA is colored as in the secondary structure diagram in (C). The twofold axis relationship between the P-loop (green) and the A-loop (purple) is evident. (**B**) A stereoview of the active site region from the direction of the polypeptide exit tunnel showing the locations of some mutations that confer antibiotic resistance. Residues are color coded in this structure and circled in (C). (**C**) Secondary structure diagram of the active site region shown in (A) and (B) color coded by region. The P-loop (green) is connected through a large region of domain V not included in these figures. Some residue numbers (with *E. coli* in parentheses) are provided along with tick marks every 10 residues. Figure generated using RIBBONS (*63*).

colleagues (*16*) found that under conditions that prevent RNA denaturation, extensive digestion of *Thermus thermophilus* 50*S* subunits with proteases followed by extraction with phenol and other agents that disrupt protein-RNA interactions did not remove several peptides from the subunit that were less than 10,000 in molecular weight. The structure makes it clear why these protein fragments were particularly resistant to protease treatments. Although protease treatment could digest the globular protein domains on the surface of the large subunit, it could not remove the long termini or loops that penetrate deeply in the 23*S* rRNA because they are sequestered within the rRNA and thus protected from cleavage.

Peptidyl transferase active site. The RNA that surrounds the substrate analogs is closely packed, much like the active site region of a protein enzyme, and the nucleotides in contact with the inhibitor are >95% conserved in all three kingdoms of life (Fig. 7). Thus, it is clear that the ribosome is a ribozyme, but what gives the RNA its catalytic power?

The residue most likely to be involved in catalysis, presumably as a general base in the first step, is A2486 (A2451), whose N3 is about 3 Å from the phosphoramide oxygen of the Yarus inhibitor that is the analog of the carbonyl oxygen of a nascent peptide bond and about 4 Å from the amide that corresponds to the amide nitrogen of the peptide bond being synthesized. Because there is no other titratable RNA functional group closer than 5 Å to the nascent peptide bond, there is no other group available to function as a general base. Ordinarily, the pK_a of the N1 of adenosine monophosphate is about 3.5 and that of its N3 is perhaps 2 pH units lower (*41*), and in order for A2486 to function as a general base, its pK_a would have to be raised to 7 or higher. The crystal structure itself suggests that its pK_a is, in fact, quite unusual. The N3 of A2486 can only hydrogen bond to the phosphate oxygen, as observed, if it (or, less likely, the phosphate oxygen) is protonated. The distance between these two atoms is about 3 Å, indicating that a hydrogen bond does, indeed, exist between them. Because the crystal is at pH 5.8, this implies that the pK_a of the N3 is >6. Muth *et al*. have measured the pK_a of the corresponding A in *E. coli* 23*S* RNA by examining its dimethyl sulfate reactivity as a function of pH and have concluded that it is 7.6, although they cannot be sure from their experiments whether it is the N3 or N1 whose pK_a they have measured (*42*). Although A2486 is protonated in our crystals at pH 5.8, at physiological pH, a significant fraction will be in the unprotonated form that can function as a general base.

There are several features of the environment of A2486 (A2451) that might affect its pK_a. It may be increased significantly in part by a charge relay mechanism, analogous to that which occurs in the active site of the serine proteases (*43*), with the buried phosphate of A2485 (A2450) performing a similar function as the buried carboxylate of Asp^{102} of chymotrypsin. The experimental 2.4 Å electron density map of the unliganded subunit (*35*) unambiguously establishes the many hydrogen bonding interactions in this critical region of the active site (Fig. 8A). The N6 of A2486 interacts with the O6 atoms of G2482 (G2447) and G2102 (G2061) (Fig. 8B). The N2 of G2482

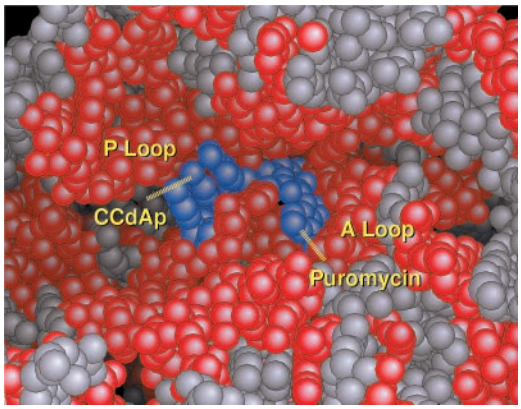

Fig. 7. Conserved nucleotides in the peptidyl transferase region with bound CCdA-p-Puro. A space-filling representation of the active site region with the Yarus inhibitor viewed down the active site cleft. All atoms belonging to 23*S* rRNA nucleotides that are >95% conserved in all three kingdoms (*44*) are colored red and all other nucleotides are white; the inhibitor is colored blue.

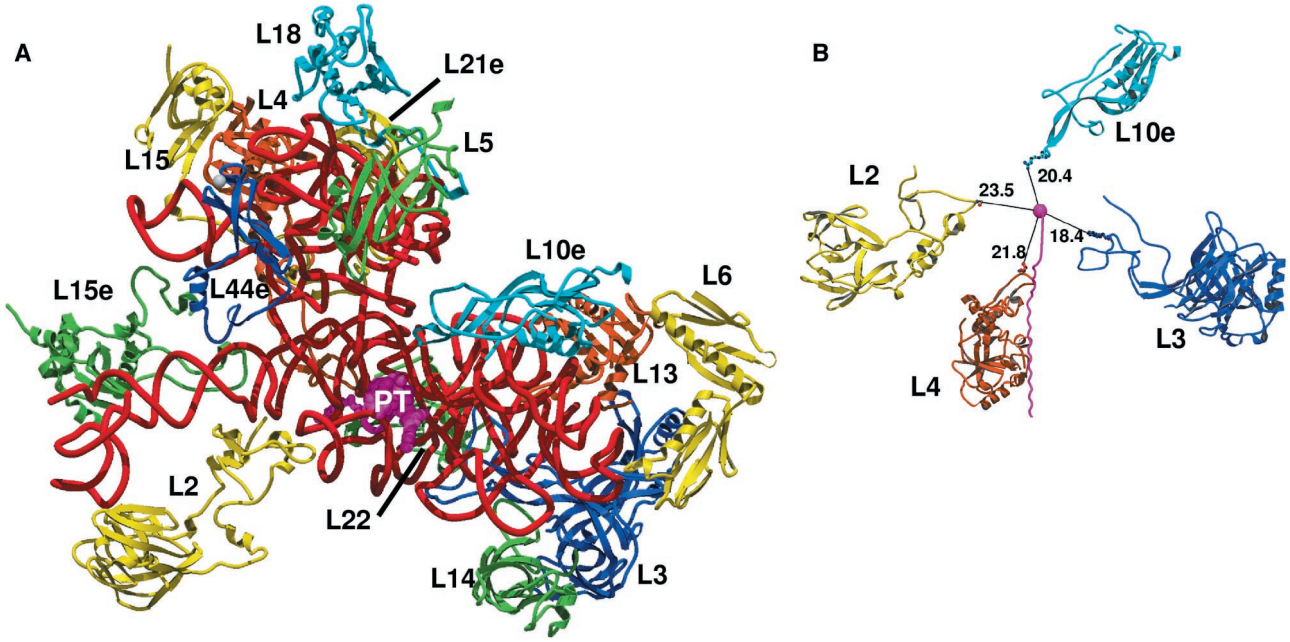

Fig. 6. The closest approach of polypeptides to the peptidyl transferase active site marked by the Yarus inhibitor, CCdA-p-Puro. (**A**) A coil representation of domain V RNA backbone in red, with the Yarus inhibitor in magenta in space-filling representation, and a ribbon backbone representation of 14 proteins that interact with that domain. (**B**) A view of the active site with the RNA removed. The phosphate of the Yarus analog and the proteins whose extensions are closest to the inhibitor are shown in ribbon with their closest side chains in all atom representation. The distances, in angstroms, between the closest protein atoms and the phosphorus analog of the tetrahedral carbon (pink) are shown, as is a modeled polypeptide product (pink).

also interacts with a nonbridging oxygen of the phosphate group of A2485 (A2450) that is among the three most solvent-inaccessible phosphate groups (826, 1497, and 2485) in the large ribosomal subunit, none of which appear to have a neutralizing counterion in the 2.4 Å resolution map. There is weak electron density that may correspond to a water molecule hydrogen bonded to the other nonbridging oxygen. The buried phosphate of A2485 could be acting electrostatically through a low-dielectric medium to affect the pK_a of A2486. Alternatively, it could abstract the proton from the exocyclic N2 of G2482 in order to neutralize its energetically unfavorable buried negative charge. This, in turn, would stabilize the otherwise rare imino tautomer of that base. The interaction of the amino tautomer of G2482 with A2486 could likewise stabilize the imino tautomer of A2486 that would result in a negative charge on its N3 were it unprotonated (Fig. 8C). In this way, some of the negative electrostatic charge originating on the buried phosphate of A2485 could be relayed to the N3 of A2486, thereby increasing its pK_a.

The A2486 (A2451) and G2102 (G2061) are completely conserved in ribosomes from all three kingdoms. Although G2482 (G2447) is >98% conserved, it is not 100% conserved. It is an A in three archaea 23*S* rRNA sequences and deleted in some eubacteria sequences (*44*). It is not possible, however, to simply replace the base of G2482 by that of an adenine and maintain the same structure

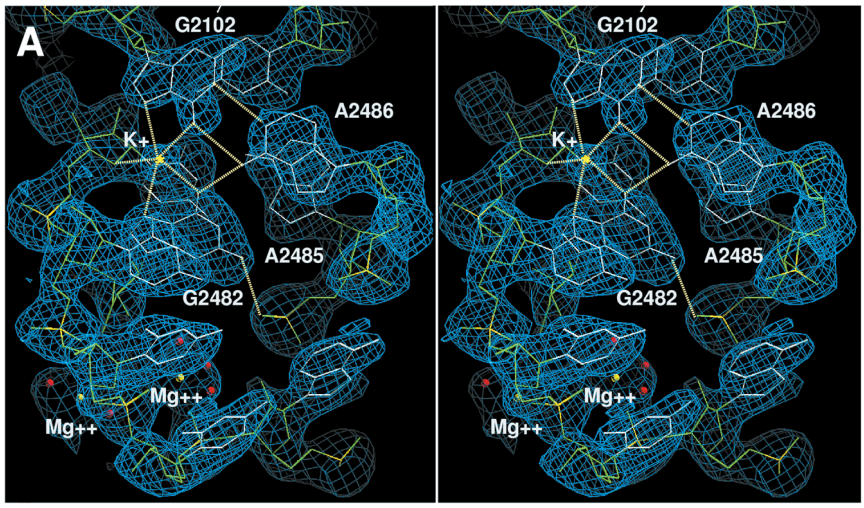

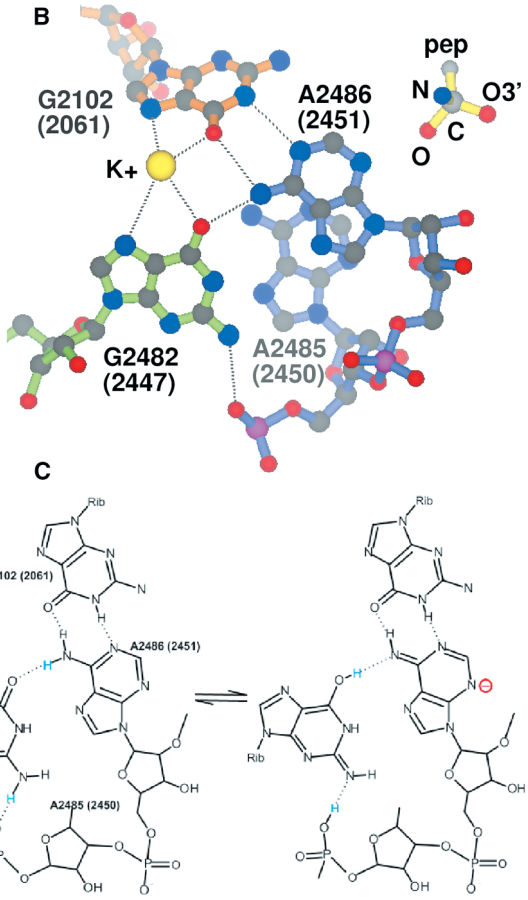

Fig. 8. The catalytic apparatus of the peptidyl transferase active site. (**A**) Stereoview shows a portion of the experimental 2.4 Å resolution electron density map (*33*) of the large subunit in the region of the catalytic site. The structure of RNA involved in interactions with A2486 is superimposed. Residues G2102 (G2061) and G2482 (G2447) are hydrogen bonded to the N6 of A2486 (A2451) and G2482, which interacts with a neighboring phosphate group of A2485 (A2450). Mg^{2+} ions are represented by yellow spheres, and their hydrating water by red spheres. A K^+ ion interacting with G2102 and G2482 is shown as a yellow sphere. (**B**) A skeletal representation with dashed hydrogen bonds showing G2482, G2102, and A2486, as well as the buried phosphate that may result in a charge relay through G2482 to the N3 of A2486. (**C**) The normal and rarer imino tautomeric forms of G2482 and A2486 that could be stabilized by the buried phosphate of residue 2485.

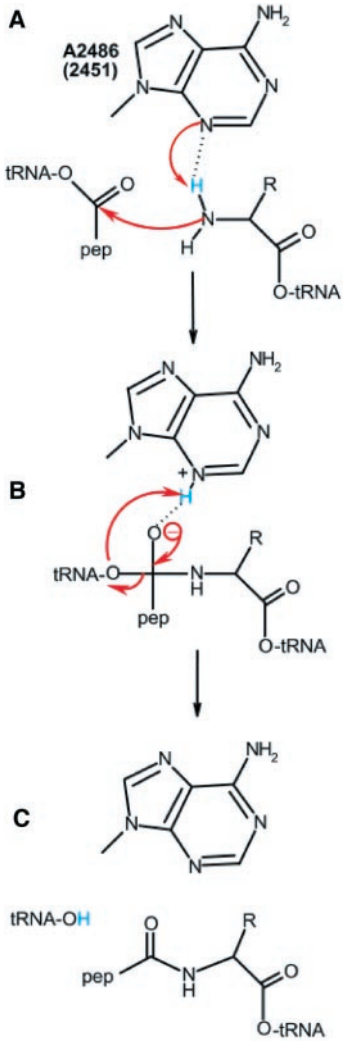

Fig. 9. A proposed mechanism of peptide synthesis catalyzed by the ribosome. A2486 (A2451) is shown as the standard tautomer in all steps, but could be represented as the imino tautomer, which would have a negative unprotonated N3 and a neutral protonated N3. We expect that the electronic distribution is actually between these two extremes. (**A**) The N3 of A2486 abstracts a proton from the αNH_2 group as the latter attacks the carbonyl carbon of the peptidyl-tRNA. (**B**) A protonated N3 stabilizes the tetrahedral carbon intermediate by hydrogen bonding to the oxyanion. (**C**) The proton is transferred from the N3 to the peptidyl tRNA 3′ OH as the newly formed peptide deacylates. Among the variations on this mechanism that should be considered would be a protonated A2486 stabilizing the intermediate, as in (B), with less contribution on acid-base catalysis, as shown in (A) and (C).

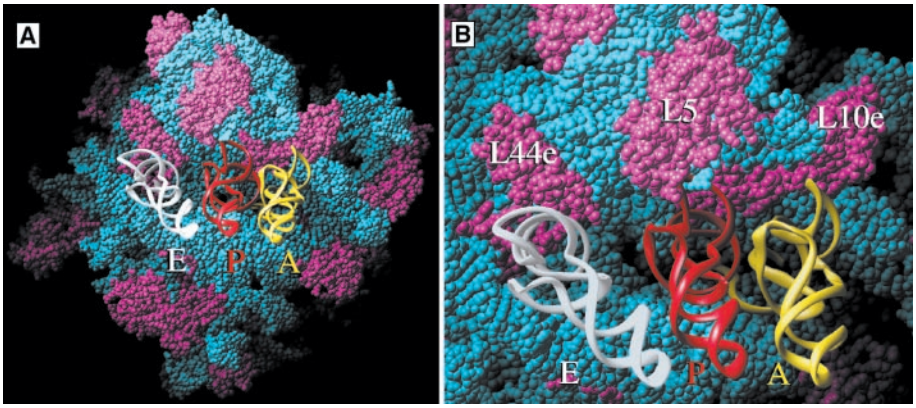

Fig. 10. A space-filling representations of the 50*S* ribosomal subunit with the 3 tRNA molecules, in the same relative orientation that they are found in the 70*S* ribosome structure by Noller and colleagues (*37*), docked by model building onto the CCA's bound in the A- and P-site. The proteins are in pink and the rRNA in blue. A backbone ribbon representation of the A-, P-, and E-sites are shown in yellow, red, and white, respectively. (**A**) The whole subunit in a rotated crown view. (**B**) A closer view shows the numbered proteins close to the tRNAs.

of the active site residues shown in Fig. 8. We expect that the positioning as well as the chemical characteristics of A2486 (A2451) must remain similar in all ribosomes. Two possible explanations for this lack of complete conservation are apparent. One possibility is sequencing errors or misalignments of sequences. Alternatively, ribosomes containing a base other than G2482 (G2447) may show additional sequence covariances that would allow G2482 to be replaced by an A in such a manner that the A could make the same kinds of hydrogen bonding interactions and tautomeric shifts as the G does.

A second feature of the environment of the catalytic site that may affect its stability, tautomeric state, and electrostatic charge distribution is a bound monovalent cation. A potassium ion interacts with the O6 and N7 atoms of G2482 and G2102 as well as with another bases. Its identity as a potassium ion is established by its coordination and by an independent experiment showing that a rubidium ion can bind to this site. The monovalent ion might also stabilize nonstandard tautomers, but the influence it might exert on the pK_a of A2486 is less obvious. Early biochemical experiments have shown the importance of potassium for peptidyl transferase activity (*3, 4*), and this binding site could be responsible for that effect.

It may also be the case that stabilization of an imino tautomer by a buried phosphate explains the expected higher pK_a of a catalytic cytosine in the active site of the hepatitis delta virus ribozyme (*45–47*). In this case, a backbone phosphate, whose solvent accessibility is similar to that of A2485 (A2450) in the ribosome, is observed to hydrogen bond to the N4 of C, and the protonated form of the imino tautomer of that C would neutralize the phosphate, promoting the function of its N3 as a general acid (*46, 47*).

Catalytic mechanism of peptide bond formation. The proximity of the N3 of A2486 (A2451) to the peptide bond being synthesized and the nature of the reaction catalyzed suggest a chemical mechanism of peptide synthesis that is analogous to the reverse of the acylation step seen in serine proteases during peptide hydrolysis (*43, 48*). In that mechanism, the basic form of His^{57} abstracts a proton from the α-amino group of the peptide hydrolysis product as it attacks the acyl-Ser^{195}. Formation of the tetrahedral carbonyl carbon intermediate is stabilized by interaction of the oxyanion formed with backbone amides (the "oxyanion hole"). Finally, His^{57} transfers the proton acquired from the αNH_2 to Ser^{195} as the tetrahedral intermediate breaks down.

We suggest that A2486 (A2451) is the analog of His^{57} in chymotrypsin and that the peptidyl-tRNA is analogous to acyl-Ser^{195}. Thus, the N3 of A2486, with its greatly elevated pK_a, abstracts a proton from the α-amino group of the A-site–bound aa-tRNA, facilitating the nucleophilic attack of this amino group on the carbonyl carbon that acylates the 3′ OH of the tRNA in the P-site (Fig. 9A). In contrast to the serine proteases, however, the oxyanion of the tetrahedral intermediate is near to the protonated N3 of A2486 (A2451) rather than being proximal to a separate oxyanion binding site. Thus, it could be that the protonated N3 of A2486 stabilizes the formation of the oxyanion by hydrogen bonding to it (Fig. 9B), as we observe in the Yarus inhibitor complex. The N3 of A2486 could then subsequently transfer its proton to the 3′ hydroxyl of the P site–bound tRNA, which is liberated as the peptide shifts to the A site–bound tRNA (Fig. 9C).

How is the catalyzed hydrolysis of the peptidyl tRNA in the P-site prevented prior to the delivery of the next appropriate aa-tRNA to the A-site? It appears from this complex that water would not be excluded from access to the peptidyl link to the P-site tRNA if the A-site were vacant. An analogous problem was discussed by Koshland in the 1960s (*49*): he asked why hexokinase does not hydrolyze ATP in the absence of glucose, because water should bind perfectly well to the binding site used by the 6-hydroxyl of glucose. The answer he proposed was induced fit; hexokinase is not catalytically competent until glucose binds and produces a conformational change that orients substrates and catalytic groups optimally. This is indeed the case (*50*). Similarly, it could be either that the catalytic A2486 and/or the peptidyl substrate are not properly oriented or that the binding site for the αNH2 group is blocked by a reoriented ribosome base in the absence of aa-tRNA in the A-site. We observe that the base of U2620 is close to A2486 in the ligand free structure, and it may serve as the plug that prevents spontaneous hydrolysis of peptidyl-tRNA. The structure of an analog of peptidyl-tRNA bound to the P-site of the large ribosomal subunit will have to be determined in order to answer this question.

Thus, it appears that this RNA enzyme uses the same principles of catalysis as a protein enzyme. First, a large catalytic enhancement is achieved by precisely orienting the two reactants, the αNH_2 from the A-site aa-tRNA and the carbonyl carbon from the P-site peptidyl-

Fig. 11. (**opposite page**) The polypeptide exit tunnel. (**A**) The subunit has been cut in half, roughly bisecting its central protuberance and its peptide tunnel along the entire length. The two halves have been opened like the pages of a book. All ribosome atoms are shown in space-filling representation, with all RNA atoms that do not contact solvent shown in white and all protein atoms that do not contact solvent shown in green. Surface atoms of both protein and RNA are color-coded with carbon yellow, oxygen red, and nitrogen blue. A possible trajectory for a polypeptide passing through the tunnel is shown as a white ribbon. PT, peptidyl transferase site. (**B**) Detail of the polypeptide exit tunnel showing distribution of polar and nonpolar groups, with atoms colored as in (A), the constriction and bend in the tunnel formed by proteins L4 and L22 (green patches close to PT), and the relatively wide exit of the tunnel. A modeled polypeptide is in white. (**C**) The tunnel surface is shown with backbone atoms of the RNA color coded by domain. Domains I (yellow), II (light blue), III (orange), IV (green), V (light red), 5*S* (pink), and proteins are blue. (**D**) A space-filling representation of the large subunit surface at the tunnel exit showing the arrangement of proteins, some of which might play roles in protein secretion. The RNA is in white (bases) and orange (backbone) and the numbered proteins are blue. A modeled polypeptide is exiting the tunnel in red. (**E**) A closer view of the half of the exit tunnel showing the relationship of the peptidyl transferase center (PT) to proteins L4 and L22 (blue). The Yarus inhibitor and a modeled peptide are red, and the 23*S* rRNA is in orange and white. (**F**) Secondary structure schematic of 23*S* rRNA identifying the sequences that approach the tunnel in red.

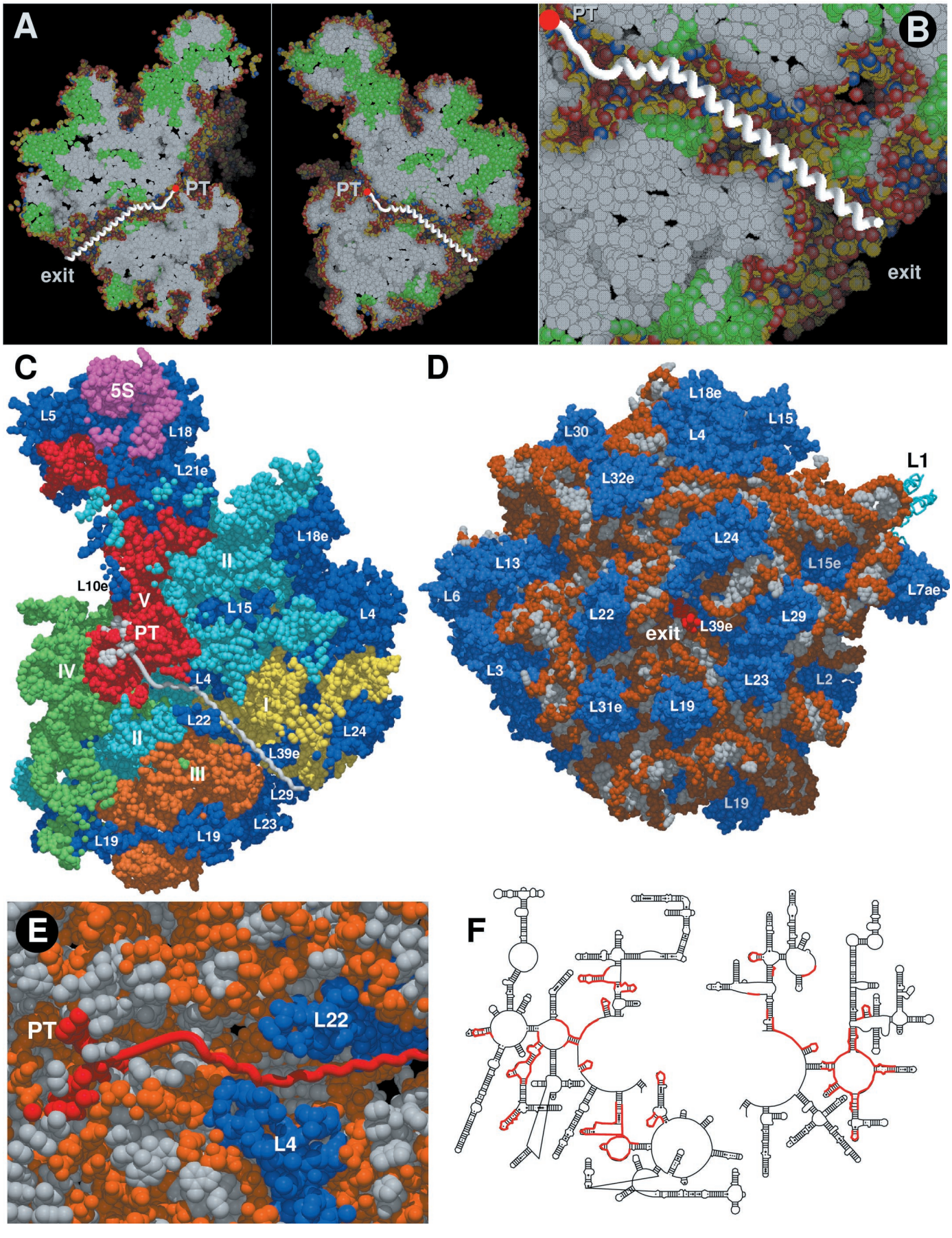
A
PT
exit
PT
B
PT
exit
C
5S
L5
L18
L21e
L18e
II
L10e
V
L15
L4
PT
IV
L4
I
L22
L24
II
L39e
III
L29
L23
L19
L19
D
L18e
L15
L30
L4
L1
L32e
L24
L13
L15e
L7ae
L6
L22
exit
L39e
L29
L3
L23
L2
L31e
L19
L19
E
PT
L22
L4
F

tRNA. This is accomplished, in part, by the interactions of the CCA ends of the A- and P-site tRNAs with the A- and P-loop, respectively. Secondly, acid-base catalysis and transition state stabilization are achieved by an enzyme functional group [A2486 (A2451) in this case] whose chemical properties are altered appropriately by the active site environment. Third, similar chemical principles may be used by RNA and protein enzymes to alter the pK_a values of functional groups. A buried carboxylate of Asp^{102} acting through His^{57} alters the nucleophilicity of Ser^{195} in chymotrypsin (*43*). In the ribosome, a solvent inaccessible phosphate may likewise act through G2482 (G2447) to alter the nucleophilicity of the N3 of A2486 (A2451). It appears that RNA molecules "learned" how to use the chemical principles of catalysis significantly before protein molecules did.

tRNA binding. Although it is not possible experimentally to bind tRNA molecules to either the A- or P-sites in these crystals for steric reasons, it is possible by model building to place the A-, P-, and E-site tRNA molecules on the large ribosomal subunit in the same relative orientation that Cate *et al.* observed in their 7.8 Å resolution crystallographic study of the *Thermus aquaticus* 70*S* ribosome (*51*). The coordinates of the three tRNA molecules in the relative positions seen in the 70*S* ribosome can be docked on the *Haloarcula marismortui* large ribosomal subunit in a way that avoids steric clashes and places the acceptor stems of the A- and P-site tRNAs near the positions of the CCAs we have observed bound to the A- and P-loops (Fig. 10). Although Cate *et al.* (*51*) modeled nucleotides C74 and C75 of the P-site tRNA in a different conformation than that observed here, the C74 residues from the CCAs in both the A- and P-sites can be connected to residue 72 of the docked A- and P-site tRNAs through a modeled residue 73, and it appears that the tRNA molecules fit well onto the surface of the subunit. Unexpectedly, this modeling places the E site–, P site–, and A site–bound tRNA molecules in close proximity to three ribosomal proteins (Fig. 10). Proteins L5 and L10e are near tRNAs in the P- and A-sites, respectively. Because both of these proteins also interact with 5*S* rRNA, this observation raises the possibility that 5*S* rRNA and some of its associated proteins might help stabilize the positioning of ribosome-bound tRNAs and is consistent with the fact that 5*S* rRNA enhances ribosomal activity, but is not absolutely essential for it (*52*). The most extensive protein interaction appears to be between L44e and the E-site tRNA and may contribute to E-site activity. This docking model suggests that the A-site tRNA interacts with the highly conserved stem-loop 2502–2518 (2467–2483). This loop together with L10e forms a large concave surface that contacts the tRNA on the T-stem, utilizing the exact same binding site exploited by EF-Tu (*53*).

Examination of the relationships between the CCAs bound in the A- and P-sites and the tRNAs to which they are connected, as well as their interactions with the ribosome, also leads to some insights into translocation. Immediately after formation of the new peptide bond and deacylation of the P-site tRNA, the acceptor end of the P-site tRNA is known to move to the E-side and that of the A-site tRNA moves to the P-site (*54*). The approximate modeling of the three tRNA molecules on the large subunit suggests some possible contributions to this process. First, there are two base-pairs between the P-site tRNA and the P-loop and only one between the A-site and the A-loop. Moving from the A- to the P-site increases base-pairing, though there must be a concomitant attraction of the deacylated P-site tRNA to an E-site. Further, the CCAs bound to the A and P loops are related by 180° rotation (Figs. 3B and 5A), whereas the tRNAs to which they are attached are not. Thus, the relationships between these CCAs and the acceptor stems to which they are attached cannot be the same in both sites and may not be equally stable. If the conformation of the A-site tRNA is less stable, then moving a tRNA from the A- to the P-site would be energetically favored.

Polypeptide exit tunnel. It appears very likely from the structure that all nascent polypeptides pass through the exit tunnel before emerging from the ribosome, because there appears to be no other way out. We are now able to address two important questions about the functioning of the polypeptide exit tunnel: (i) Why do nascent proteins not stick to its walls? Teflon has the marvelous property of not sticking to denatured egg proteins, so how has the ribosome achieved a similar nonstick surface for the denatured proteins that must pass through the tunnel? (ii) Do proteins fold to any degree in the tunnel, giving the ribosome a chaperon-like function?

The length of the tunnel from the site of peptide synthesis to its exit is about 100 Å, broadly consistent with the length of nascent polypeptide that is protected from proteolytic cleavage by the ribosome (*55*), and the minimum length required for antibody recognition at the exit (*56*). The tunnel is largely straight, except for a bend 20 to 35 Å from the peptidyl transferase center (Fig. 11). Its diameter varies from about 20 Å at its widest to a narrow point of about 10 Å at the very beginning and again at a position 28 Å from the tunnel exit. The average diameter is about 15 Å. Because the smallest orifice through which the polypeptide product must pass only barely accommodates the diameter of an α-helix, it seems unlikely that significant protein folding could occur within the ribosome beyond the formation of α-helix.

The majority of the tunnel surface is formed by domains I through V of 23*S* rRNA, but significant contributions are also made by the nonglobular regions of proteins L4, L22, and L39e, which not only fill some of the voids in the RNA scaffold, but also form significant portions of the tunnel wall (Fig. 11). The largest protein contributor to the surface of the tunnel is L22, whose long β-hairpin loop lies between RNA segments of domains I through IV and is approximately parallel with the axis of the tunnel. Unlike the other tunnel proteins, protein L39e does not have a globular domain at the surface of the particle and is almost entirely buried in domains I and III underneath protein L23. Interestingly, the nucleotides of 23*S* rRNA that form the tunnel wall are predominantly from loops in the 23*S* rRNA secondary structure (Fig. 11). As it progresses through the tunnel from the active site, a nascent polypeptide first encounters domain V, followed 20 Å further along by domains II and IV and proteins L4 and L22. The last half of the tunnel is formed by domains I and III and the protein L39e.

The narrowest part of the tunnel is formed by proteins L22 and L4, which approach the tunnel from opposite sides, forming what appears to be a gated opening (Fig. 11C). The function of this constriction, if any, is not ob-

Table 1. Statistics for data collection and scaling.

Crystal	Native A	Native B	CCdAp-Puro	Mini-helix
Soak time (hours)	–	–	24	24
Soak concentration (μM)	–	–	100	100
Wavelength (Å)	1.0	1.0	1.0	1.0
Observations	1,571,171	1,344,877	2,590,726	2,712,813
Unique	284,533	369,167	367,284	447,121
Redundancy	5.5	3.6	7.0	6.0
Resolution limits (Å)	70.0–3.2	70.0–3.0	70.0–3.0	70.0–2.8
(High-resolution bin)*	(3.26–3.20)	(3.05–3.00)	(3.23–3.17)	(3.08–3.02)
Completeness	94.1 (96.0)	98.9 (99.3)	98.6 (99.9)	99.6 (100)
I/σI	14.6 (4.0)	10.8 (3.1)	11.0 (2.8)	10.7 (2.9)
R_{merge}†	10.2 (40)	11.5 (38)	18.8 (84)	14.3 (72)
R_{iso} Native A‡	–	–	6.8 (20.8)	14.4 (25.2)
R_{iso} Native B‡	–	–	12.6 (27.4)	17.5 (31.0)

*Statistics in parenthesis are calculated for the high-resolution bin used in map calculations, which, as indicated, was sometimes lower in resolution than the high-resolution bin used in data reduction. †R_{merge}: $\Sigma\Sigma_i|I_{(h)} - I_{(h)i}|/\Sigma\Sigma I_{(h)i}$, where $I_{(h)}$ is the mean intensity after reflection. ‡R_{iso}: $\Sigma|F_{PH} - F_P|/\Sigma F_{PH}$, where F_{PH} and F_P are the soaked and the native crystal structure factor amplitudes, respectively.

vious. It might be the place where the nature of the nascent chain is sensed, and that information is then transmitted to the surface of the particle, perhaps through L22 or L4. The β-hairpin of L22 at the site of this orifice and the 23*S* rRNA interacting with it are highly conserved; its globular portion is located adjacent to the tunnel exit on the surface that must face the translocon during protein secretion (Fig. 11).

The "nonstick" character of the tunnel wall must reflect a lack of structural and polarity complementarity to any protein sequence or conformation that it encounters. The tunnel surface is largely hydrophilic and includes exposed hydrogen bonding groups from bases, backbone phosphates, and polar protein side chains (Fig. 11). Although there are many hydrophobic groups (sugars, bases, protein side chains) facing the tunnel as well, there are no patches of hydrophobic surface large enough to form a significant binding site for hydrophobic sequences in the nascent polypeptide. Because the tunnel is some 15 Å in diameter and filled with water and the newly synthesized polypeptide is presumably freely mobile, the binding of a peptide to the tunnel wall would result in a large loss of entropy that would have to be compensated for by a large complementary interaction surface that is larger than 700 Å (*57*). Similarly, while Arg and Lys side chains from a nascent peptide may indeed interact with the phosphates exposed in the tunnel, the degree of structural complementarity and the net binding energy obtained after displacing bound counterions must be too small to overcome the large unfavorable entropy of immobilization that would result from peptide binding. Thus, although the ribosome tunnel is made primarily of RNA, the nature of its surface is reminiscent of the interior surface of the chaperonin, GroEl (*58*) in its nonbinding conformation. Only in the conformation that exposes a large hydrophobic surface does GroEL bind denatured protein.

There are six proteins (L19, L22, L23, L24, L29, and L31e) located at the exit from the tunnel, facing the translocon onto which the ribosome docks during protein secretion. Although there is good evidence that the ribosome binds to the translocon even after extensive digestion of its protein by protease, implying that interaction between the translocon and the ribosome is mediated by RNA (*59*), the proximity of these proteins to the translocon leads us to wonder what role, if any, they might play in the protein secretion process. Recent data from the Dobberstein laboratory shows that the NH_2-terminal domain of SRP54, the G protein from the signal recognition particle involved in signal peptide binding, can be crosslinked to ribosomal proteins L23 and L29 (*60*). These two proteins are adjacent to each other and at the tunnel exit (Fig. 11).

Evolution. In vitro evolution of RNA oligonucleotides has produced small RNA molecules that can bind molecules like the Yarus inhibitor effectively or catalyze the peptidyl transfer reaction (*61, 62*). The sequence and secondary structure of one of these selected RNAs is reminiscent of the peptidyl tranferase loop in domain V of 23*S* rRNA (*61*). The most striking similarity is a five-nucleotide sequence that is identical to a sequence in domain V that includes the catalytic A2486, G2482, and the buried phosphate of A2485. Remarkably, all of the groups involved in the proposed charge relay system for activating A2486 in the ribosome are present in the in vitro–selected ribozyme. Thus, although the surrounding structural context is likely to be different, it seems plausible that this artificially evolved ribozyme uses the same mechanisms as the ribosome for shifting the pK_a of an adenine and likewise uses it as a base for peptide synthesis. The second RNA (*62*), which binds the Yarus inhibitor, contains a 12-nucleotide loop that includes a nine-base sequence identical to that found in the A2486 region of the peptidyl transferase loop.

The striking similarities between the sequences containing the key catalytic elements found in the peptidyl-transferase active site of the ribosome and the sequences of in vitro–selected RNAs having related activities make it clear that the appearance of a small RNA domain capable of catalyzing peptidyl transferase was a plausible first step in the evolution of protein synthesis on the ribosome. The first peptides synthesized by this primordial peptide synthesizing enzyme might have been random polymers or copolymers, and it may have functioned with substrates as simple as an aminoacylated CCA. Basic peptides of the types observed to form the nonglobular extensions that co-fold with the 23*S* rRNA might have been among the first peptides synthesized that were functionally useful. Such peptides could have enhanced the stability of the protoribosome and other early ribozymes as the more sophisticated peptides of the present-day ribosome appear to do. The evolution of this simple peptide-synthesizing domain into a ribonucleoprotein many times larger and capable of messenger-directed synthesis required many additional steps that are not yet obvious.

References and Notes

1. R. R. Traut and R. E. Monro, *J. Mol. Biol.* **10**, 63 (1964).
2. I. Rychlik, *Biochim. Biophys. Acta* **114**, 425 (1966).
3. R. E. Monro, *J. Mol. Biol.* **26**, 147 (1967).
4. B. E. H. Maden, R. R. Traut, R. E. Monro, *J. Mol. Biol.* **35**, 333 (1968).
5. H. F. Noller, *Annu. Rev. Biochem.* **53**, 119 (1984).
6. B. Wittmann-Liebold *et al.*, in *The Ribosome: Structure, Function, & Genetics*, W. E. Hill *et al.*, Eds. (American Society for Microbiology, Washington, DC, 1990), pp. 598–616.
7. J. Ofengand, in *Ribosomes: Structure, Function and Genetics*, G. Chambliss *et al.*, Eds. (University Park Press, Baltimore, MD, 1980), pp. 497–530.
8. B. S. Cooperman, in (*7*), pp. 531–554.
9. C. Guerrier-Takada, K. Gardiner, T. Marsh, N. Pace, S. Altman, *Cell* **35**, 849 (1983).
10. K. Kruger *et al.*, *Cell* **31**, 147 (1982).
11. F. H. C. Crick, *J. Mol. Biol.* **38**, 367 (1968).
12. A. Barta, G. Steiner, J. Brosius, H. F. Noller, E. Kuechler, *Proc. Natl. Acad. Sci. U.S.A.* **81**, 3607 (1984).
13. B. Vester and R. A. Garrett, *EMBO J.* **7**, 3577 (1988).
14. H. F. Noller, *Annu. Rev. Biochem.* **60**, 191 (1991).
15. R. A. Garrett and C. Rodriguez-Fonseca, in *Ribosomal RNA: Structure, Evolution, Processing and Function in Protein Biosynthesis*, R. A. Zimmermann and A. E. Dahlberg, Eds. (CRC Press, Boca Raton, FL, 1996), pp. 327–355.
16. H. F. Noller, V. Hoffarth, L. Zimniak, *Science* **256**, 1416 (1992).
17. P. Khaitovich, A. S. Mankin, R. Green, L. Lancaster, H. F. Noller, *Proc. Natl. Acad. Sci. U.S.A.* **96**, 85 (1999).
18. F. J. Franceschi and K. H. Nierhaus, *J. Biol. Chem.* **265**, 6676 (1990).
19. R. Green and H. F. Noller, *Annu. Rev. Biochem.* **66**, 679 (1997).
20. I. Nitta, T. Ueda, K. Watanabe, *RNA* **4**, 257 (1998).
21. I. Nitta, Y. Kamada, H. Noda, T. Ueda, K. Watanabe, *Science* **281**, 666 (1998).
22. P. Khaitovich, T. Ternson, A. S. Mankin, R. Green, *RNA* **5**, 605 (1999).
23. R. A. Milligan and P. N. T. Unwin, *Nature* **319**, 693 (1986).
24. A. Yonath, K. R. Leonard, H. G. Wittmann, *Science* **236**, 813 (1987).
25. C. Bernabeu and J. A. Lake, *Proc. Natl. Acad. Sci. U.S.A.* **79**, 3111 (1982).
26. L. A. Ryabova, O. M. Selivano, V. I. Baranov, V. D. Vasiliev, A. S. Spirin, *FEBS Lett.* **226**, 255 (1988).
27. R. Beckmann *et al.*, *Science* **278**, 2123 (1997).
28. J. Frank *et al.*, *Nature* **376**, 441 (1995).
29. J. Frank *et al.*, *Biochem. Cell Biol.* **73**, 757 (1995).
30. H. Stark *et al.*, *Cell* **88**, 19 (1997).
31. H. Stark *et al.*, *Structure* **3**, 815 (1995).
32. M. Welch, J. Chastang, M. Yarus, *Biochemistry* **34**, 385 (1995).
33. D. Moazed and H. F. Noller, *Proc. Natl. Acad. Sci. U.S.A.* **88**, 3725 (1991).
34. E. Monro, M. L. Celma, D. Vazquez, *Nature* **222**, 356 (1969).
35. N. Ban, P. Nissen, J. Hansen, P. B. Moore, T. A. Steitz, *Science* **289**, 905 (2000).
36. D. Moazed and H. F. Noller, *Cell* **57**, 585 (1989).
37. D. F. Kim and R. Green, *Mol. Cell* **4**, 859 (1999).
38. Crystals of 50*S* ribosomal subunits were grown and stabilized as described (*35*). CCdA-p-puromycin (Fig. 1A) was a generous gift from Michael Yarus (*32*). *N*-amino-acylated mini-helices (Fig. 1B) were synthesized by Dharmacon. Following deprotection, oligonucleotides were briefly heated to 100°C and snap-cooled on ice to reanneal. Ribosomal 50*S* subunit crystals were stabilized and then soaked for 24 hours in stabilization buffer plus 100 μM CCdA-p-puromycin or *N*-amino-acylated mini-helices before cryovitrification in liquid propane and x-ray diffraction data collection. Phases were calculated by density modification (crystallographic and NMR system) beginning with the best experimental phases (*35*) using $2F_o$(analog) – F_o(native) for amplitudes, from 60.0 to 3.2 Å. Native amplitudes were from the most isomorphous native 1 data set, except for those amplitudes that were present only in the more complete native 2 data set. Calculated $2F_o - F_o$ amplitudes that were less than twice the corresponding calculated σ were replaced by F_o(analog). Maps were then calculated using phases from density modified and $2F_o$(analog) – F_o(native) or F_o(analog) – F_o(native) amplitudes.
39. R. R. Samaha, R. Green, H. F. Noller, *Nature* **377**, 309 (1995).
40. R. Green, C. Switzer, H. F. Noller, *Science* **280**, 286 (1998).
41. W. Saenger, *Principles of Nucleic Acid Structure*, C. R. Cantor, Ed., Springer Advanced Texts in Chemistry (Springer-Verlag, New York, 1984).
42. G. W. Muth, L. Ortoleva-Donnelly, S. A. Strobel, *Science* **289**, 947 (2000).
43. D. M. Blow, J. J. Birktoft, B. S. Hartley, *Nature* **221**, 337 (1969).
44. R. R. Gutell *et al.*, in preparation (data can be found at www.rna.icmb.utexas.edu.)

45. A. Ferre-D'Amare, K. Zhou, J. A. Doudna, *Nature* **395**, 567 (1998).
46. S. Nakano, D. M. Chadalavada, P. C. Bevilacqua, *Science* **287**, 1493 (2000).
47. A. T. Perrotta, I.-h. Shih, M. D. Been, *Science* **286**, 123 (1999).
48. T. A. Steitz and R. G. Shulman, *Annu. Rev. Biophys. Bioeng.* **11**, 419 (1982).
49. D. E. Koshland Jr., *Cold Spring Harbor Symp. Quant. Biol.* **28**, 473 (1963).
50. W. S. Bennett Jr. and T. A. Steitz, *Proc. Natl. Acad. Sci. U.S.A.* **75**, 4848 (1978).
51. J. H. Cate, M. M. Yusupov, G. Z. Yusupova, T. N. Earnest, H. F. Noller, *Science* **285**, 2095 (1999).
52. P. B. Moore, in *Ribosomal RNA & Structure, Evolution, Processing and Function in Protein Biosynthesis*, R. A. Zimmermann and A. E. Dahlberg, Eds. (CRC Press, Boca Raton, FL, 1996), pp. 199–236.
53. P. Nissen, M. Kjeldgaard, S. Thirup, B. F. C. Clark, J. Nyborg, *Biochimie* **78**, 921 (1996).
54. D. Moazed and H. F. Noller, *Nature* **342**, 142 (1989).
55. W. D. Picking, W. L Picking, O. W. Odonu, B. Hardesty, *Biochemistry* **31**, 2368 (1992).
56. G. Blobel and D. D. Sabatini, *J. Cell. Biol.* **45**, 130 (1970).
57. C. Chothia and J. Janin, *Nature* **256**, 705 (1975).
58. Z. Xu and P. B. Sigler, *J. Struct. Biol.* **124**, 129 (1998).
59. A. Prinz, C. Behrens, T. A. Rapoport, E. Hartmann, K.-U. Kalies, *EMBO J.* **19**, 1900 (2000).
60. B. Dobberstein, personal communication.
61. B. Zhaug and T. R. Cech, *Chem. Biol.* **5**, 539 (1998).
62. M. Welch, I. Majerfeld, M. Yarus, *Biochemistry* **36**, 6614 (1997).
63. M. Carson, *Methods Enzymol.* **227**, 493 (1997).
64. We thank B. Freeborn for her skilled technical assistance in preparing 50*S* ribosomal subunit material and crystals. We thank M. Yarus for his generous gift of CCdA-p-puromycin, and S. Strobel, J. Steitz, D. Crothers, D. Herschlag, and T. Cech for discussions. We are indebted to R. Sweet and M. Capel for their assistance with data collection at the National Synchrotron Light Source (Brookhaven National Laboratory), and A. Joachimiak and the staff of 19-ID at the Advanced Photon Source (Argonne National Laboratory). Supported by grants from NIH to T.A.S. (GM22778) and P.B.M. (GM54216) and a grant from the Agouron Institute to T.A.S. and P.B.M. N.B. is supported by a Burroughs Welcome Fund Career Award. Coordinates of the ligand-free subunit and of domain V complexed with the two analogs have been deposited in the Protein Data Bank with accession numbers 1FFK, 1FFZ, and 1FG0.

10 July 2000; accepted 24 July 2000

Magnetic Vortex Core Observation in Circular Dots of Permalloy

T. Shinjo,[1]* T. Okuno,[1] R. Hassdorf,[1]† K. Shigeto,[1] T. Ono[2]

Spin structures of nanoscale magnetic dots are the subject of increasing scientific effort, as the confinement of spins imposed by the geometrical restrictions makes these structures comparable to some internal characteristic length scales of the magnet. For a vortex (a ferromagnetic dot with a curling magnetic structure), a spot of perpendicular magnetization has been theoretically predicted to exist at the center of the vortex. Experimental evidence for this magnetization spot is provided by magnetic force microscopy imaging of circular dots of permalloy ($Ni_{80}Fe_{20}$) 0.3 to 1 micrometer in diameter and 50 nanometers thick.

Ferromagnetic materials generally form domain structures to reduce their magnetostatic energy. In very small ferromagnetic systems, however, the formation of domain walls is not energetically favored. Specifically, in a dot of ferromagnetic material of micrometer or submicrometer size, a curling spin configuration—that is, a magnetization vortex (Fig. 1)—has been proposed to occur in place of domains. When the dot thickness becomes much smaller than the dot diameter, usually all spins tend to align in-plane. In the curling configuration, the spin directions change gradually in-plane so as not to lose too much exchange energy, but to cancel the total dipole energy. In the vicinity of the dot center, the angle between adjacent spins then becomes increasingly larger when the spin directions remain confined in-plane. Therefore, at the core of the vortex structure, the magnetization within a small spot will turn out-of-plane and parallel to the plane normal. Although the concept of such a magnetic vortex with a turned-up magnetization core has been introduced in many textbooks (*1*), direct experimental evidence for this phenomenon has been lacking.

Recent model calculations for a Heisenberg spin system of $32 \times 32 \times 8$ spins in size (*2*) indicate that a curling spin structure is realized even for a dot of square shape, where a spot with turned-up magnetization normal to the plane exists at the center of the vortex (Fig. 1). The simulations, which are based on a discrete-update Monte Carlo method described elsewhere (*3*), take account of exchange and dipole energies while neglecting anisotropy. Further, they show that no out-of-plane component of the magnetization occurs if the dot thickness becomes too small. On the other hand, when the thickness exceeds a certain limit, the top and bottom spin layers will tend to cancel each other, and again no perpendicular magnetization should be observed. A vortex core with perpendicular magnetization is therefore expected to appear if the shape, size, and thickness of the dot are all appropriate, and the anisotropy energy may be neglected.

A number of experiments have been carried out to study nanoscale magnetic systems. Cowburn *et al.* reported magneto-optical measurements on nanoscale supermalloy ($Ni_{80}Fe_{14}Mo_5$) dot arrays (*4*). From the profiles of the hysteresis loops, they concluded that a collinear-type single-domain phase is stabilized in dots with diameters smaller than a critical value (about 100 nm) and that a vortex phase likely occurs in dots with larger diameters. However, the authors were not able to obtain direct information on the spin structure in each dot. As suggested by theoretical calculations, the size of the perpendicular magnetization spot at the vortex core should be fairly small, and hence conventional magnetization measurements should fail to distinguish a fraction of perpendicular magnetization from the surrounding vortex magnetic structure.

In this context, we report magnetic force microscopy (MFM) measurements on circular dots of permalloy ($Ni_{80}Fe_{20}$) that give clear evidence for the existence of a vortex spin structure with perpendicular magnetization core. Samples of ferromagnetic dots were prepared by means of electron-beam lithography and evaporation in an ultrahigh vacuum using an electron-beam gun. The desired patterns were defined on thermally oxidized Si substrates capped by a layer of resist and subsequently topped by a layer of permalloy. By a lift-off process, the resist is removed and permalloy dots with designed sizes remain on top of the Si surface. The thickness of the circular dots reported here is 50 nm; the diameter of the dots was varied from 0.1 to 1 μm. In MFM, the instrument was operated in ac mode to detect the magnetic force acting between the cantilever tip and the surface of the permalloy dots. A low-moment ferromagnetic tip of CoCr was used to minimize the effect of stray fields. The distance between tip and sample surface was set to 80 nm on average. Sample scans

[1]Institute for Chemical Research, Kyoto University, Uji 611-0011, Japan. [2]Faculty of Science and Technology, Keio University, Yokohama 223-8522, Japan.

*To whom correspondence should be addressed. E-mail: shinjo@scl.kyoto-u.ac.jp

†Present address: Research Center Caesar, D-53111 Bonn, Germany.